Ionics
https://doi.org/10.1007/s11581-026-07213-8

RESEARCH

Doping Li-rich layered oxide cathodes with Sn or In to enhance their structural stability and electrochemical performance

Reihane Etefagh[1,2] · Amirhassan Amiri[1] · Boshra Ghanbari Shohany[1,2] · Nima Rasekh Saleh[3]

Received: 28 January 2026 / Revised: 19 April 2026 / Accepted: 20 May 2026

Abstract

$Li_{1.2}Mn_{0.54}Ni_{0.13}Co_{0.13}O_2$ (LMNCO) is known a promising high-capacity cathode material for next-generation lithium-ion batteries (LIBs), leveraging both transition-metal and oxygen redox reactions. However, challenges such as oxygen loss, structural degradation, and voltage fading hinder their practical application. To address these issues, we synthesized LMNCO cathode *via* solid-state methods and systematically investigated the effects of indium (In) or tin (Sn) dopant on its structural and electrochemical properties. X-ray diffraction (XRD) spectroscopy with Rietveld refinement confirmed the retention of the α-$NaFeO_2$ structure (*R-3 m* symmetry) in all samples with Sn or In doping inducing lattice expansion. Characterization tests revealed minimal morphological changes but altered surface chemistry and metal–oxygen bonding. Electrochemically, doped cathodes exhibited enhanced Li^+ diffusion kinetics and reduced charge-transfer resistance. Compared to undoped and In-doped cathodes, the one doped with Sn delivered better electrochemical performance where it delivered discharge capacity of 308.9 mAh/g after 10 cycles 0.1 C, attributing to facilitated Li^+ transport and lowered impedance. This study demonstrates that strategic doping with Sn or In can significantly stabilize Li-rich cathodes, offering a viable route toward high-energy, durable lithium-ion batteries.

Keywords Lithium-ion batteries · LMNCO cathode · Doping · Indium (In) · Tin (tin)

Introduction

Lithium- and manganese-rich layered oxides, especially the compound $Li_{1.2}Mn_{0.54}Ni_{0.13}Co_{0.13}O_2$ (LMNCO), have become promising cathode materials for next-generation lithium-ion batteries (LIBs) due to their high specific capacity (>250 mAh/g) and energy density (>900 Wh/kg) originating from combined redox activity of transition metals and lattice oxygen at high voltages (>4.5 V) [1–3]. This high energy performance, on the other hand, is often accompanied by some irreversible structural degradation, such as oxygen loss, cation migration, and phase changes like the transition from layered to spinel, which cause voltage drop, capacity loss, and higher impedance over time [4–6].

Researchers have focused on two main strategies to deal with these problems, including bulk doping to stabilize the crystal structure and speed up the movement of lithium ions and surface modification to improve interfacial stability and reduce side reactions. Tin (Sn) and indium (In) are two dopants which have received considerable attention because they change the electrochemical performance of cathode materials in interesting ways [7–9]. For example, Sn^{4+} doping has been shown to make the lattice structure bigger by replacing manganes ions (Mn^{4+}), making it easier for lithium ions to move around and lowers structural stress. Zhou et al. showed that presence of even a small amount of Sn (1 mol%) in Li-rich cathodes could make a big difference in the initial discharge capacity (~269 mAh/g) and cycling stability [10].

Co-doping strategies using Sn and alkali metals like potassium (K) have also been shown to improve rate capabilities and lower charge transfer resistance by making lithium pathways wider and stabilizing interfaces [11]. Also, surface coatings made of Sn-based compounds like SnO_2

✉ Amirhassan Amiri
ah.amiri@um.ac.ir

[1] Department of Chemistry, Ferdowsi University of Mashhad, Mashhad 9177948974, Iran

[2] Borhan Nano Scale Company, Mashhad, Iran

[3] Department of Mechanical and Aerospace Engineering, ET. C, Islamic Azad University, Tehran, Iran

Published online: 27 May 2026

and Li_2SnO_3 have successfully been used to prevent oxygen formation during the initial cycles, which subsequently keep the Coulombic efficiency high [12, 13].

Previous studies revealed that doping other types of LIBs cathodes like $LiFePO_4$ with In or Sn dopants could result in significant improvements in their electronic conductivity and rate performance [14, 15]. Hence, this study aims to investigate the effect of the abovementioned dopants on structure and electrochemical performance of lithium-rich layered cathodes. In this regard, three types of LMNCO cathodes, including undoped (pristine), Sn-doped, and In-doped are initially synthesized.

Then, they are structurally examined using different characterization tests. The X-ray diffraction (XRD) spectroscopy and Rietveld refinement are adopted to determine the crystal structure and lattice expansion. Field emission scanning electron microscopy (FESEM), Fourier transform infrared spectroscopy (FTIR), energy-dispersive X-ray spectroscopy (EDXS), and Raman spectroscopy are employed to scrutinize morphology and composition of fabricated cathodes. Finally, galvanostatic charge–discharge measurements, cyclic voltammetry (CV), and electrochemical impedance spectroscopy (EIS) are carried out to study electrochemical behavior of cathodes.

Experimental section

Materials

High-purity metal salts were employed for the synthesis of the target nanopowders, consisting of nickel nitrate hexahydrate ($Ni(NO_3)_2{\cdot}6\ H_2O$), cobalt nitrate hexahydrate ($Co(NO_3)_2{\cdot}6\ H_2O$), manganese nitrate tetrahydrate ($Mn(NO_3)_2{\cdot}4\ H_2O$), lithium nitrate ($LiNO_3$), and tin nitrate ($Sn(NO_3)_2$). Citric acid monohydrate ($C_6H_8O_7{\cdot}H_2O$) was added as a chelating agent to stabilize metal ions and facilitate gel formation. All chemicals were used as-received without further purification.

Synthesis methods

Synthesis of undoped LMNCO cathode

The pure nanopowder was synthesized using sol-gel method. In this regard, stoichiometric quantities of metal salts, including 1.298 g $Ni(NO_3)_2{\cdot}6\ H_2O$, 1.300 g $Co(NO_3)_2{\cdot}6\ H_2O$, 4.730 g $Mn(NO_3)_2{\cdot}4\ H_2O$, and 3.008 g $LiNO_3$, were dissolved in distilled water under constant stirring. The solution was maintained at 75–80 °C in an oil bath to complete dissolution process. Subsequently, 13.52 g of $C_6H_8O_7{\cdot}H_2O$ was introduced into solution, followed by continuous stirring until formation of a homogeneous gel. The gelation process was completed by maintaining the mixture at 80 °C for approximately 4 h. The resulting gel was then dried at 120 °C for 6 h, followed by a two-step calcination process: first at 150 °C for 5 h, and then at 850 °C for 4 h to obtain the final crystalline phase. The obtained nanopowder exhibited a uniform black coloration, indicative of the successful formation of the desired crystalline structure.

Synthesis of Sn- and In- doped LMNCO cathodes

The doped nanopowders were synthesized using a modified sol-gel method analogous to one applied for pure sample [16] with stoichiometric adjustments to incorporate dopants while maintaining charge balance. For both 5% Sn-doped and 5% In-doped variants, the cobalt nitrate hexahydrate ($Co(NO_3)_2{\cdot}6\ H_2O$) content was reduced to 1.250 g and instead, 0.300 g of either tin nitrate ($Sn(NO_3)_2$) or indium nitrate ($In(NO_3)_3$) was added, respectively, while keeping other precursors constant (1.298 g $Ni(NO_3)_2{\cdot}6\ H_2O$, 4.730 g $C_4H_6MnO_4{\cdot}4\ H_2O$, and 3.008 g $LiNO_3$). The precursors were dissolved in 30 g of distilled water under vigorous stirring until complete dissolution and then, the resultant solution was heated to 75–80 °C in an oil bath. Afterward, 13.52 g citric acid monohydrate was gradually added, followed by continuing stirring until formation of a homogeneous viscous gel, which was aged at 80 °C for 4 h to complete gelation. The gels were subsequently dried at 120 °C for 6 h, followed by a two-stage calcination process: initial heating at 150 °C for 5 h to remove organic components, and then annealing at 850 °C for 4 h to achieve crystalline phase purity, yielding black, homogeneous nanopowders with well-developed crystal structures.

Electrode fabrication, cell assembling, and electrochemical experiments

For fabrication of working electrodes used in this study, first, the slurry prepared by dispersing active material (85 wt%), polyvinylidene fluoride (PVDF) (5 wt%), and carbon black (10 wt%) in N-methyl-2-pyrrolidone (NMP) solvent was casted on aluminum foil substrate as the current collector. Afterward, the resultant electrode was dried at 120 °C for 12 h.

The CR2032 coin half-cells employed for all electrochemical analyses were composed of fabricated Li rich cathode as the working electrode and Li foil as the counter electrode. The micro-pores polypropylene membrane (Celgard 2400) was adopted in order to separate the electrodes. For preparation of electrolyte, 1 M $LiPF_6$ was dissolved in ethylene carbonate (EC)/dimethyl carbonate (DMC) (1:1,

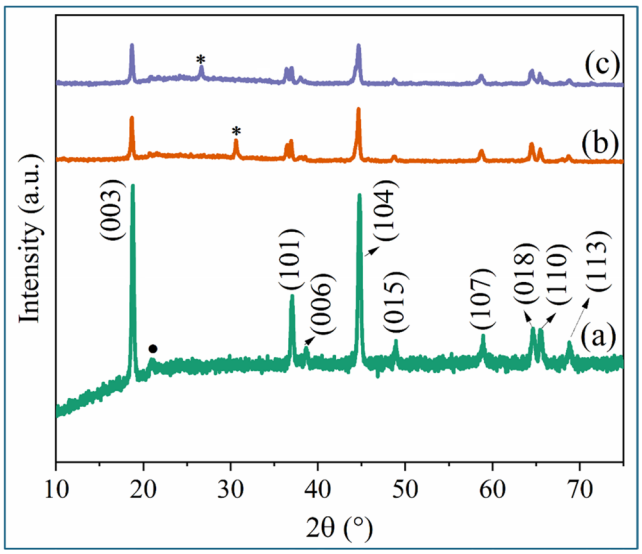

Fig. 1 XRD patterns of (**a**) undoped LMNCO cathode and its counterparts doped with (**b**) In, or (**c**) Sn dopant

v/v). The fabrication of coin half-cells was done in dry glove box filled with argon gas.

Charge and discharge capacity of Li rich cathodes were obtained with a battery tester (Neware multi-channel instrument, CT-3008). The voltage range applied for galvanostatic charge/discharge measurements was 1.8–4.8 V (versus Li/Li^+). The CV analysis was performed in the potential range of 2.0–5.0 V (versus Li/Li^+). The scan rate applied in CV was 0.5 mV/s. The EIS test was carried out after the first cycle 0.1 C using AC amplitude of 10 mV and frequency range of 100 kHz to 0.1 Hz. The CV and EIS analyses were done at room temperature by means of a Galvanostat/Potentiostat Autolab (PG-STAT 302 N).

Results and discussion

Characterization tests

Figure 1 presents XRD patterns of undoped LMNCO cathode material alongside its In- and Sn-doped counterparts. XRD analysis was employed to assess the crystallinity and determine the lattice parameters of the synthesized samples. As illustrated in Fig. 1a, distinct diffraction peaks are observed at approximately 18.8°, 37.1°, 38.6°, 44.8°, 48.9°, 58.9°, 64.6°, 65.6°, and 68.9°. These peaks are indexed according to the JCPDS reference (No. 49–0524), corresponding to the (003), (101), (006), (104), (015), (107), (018), (110), and (113) crystallographic planes, respectively. The results confirm that the undoped LMNCO cathode adopts a well-defined layered α-$NaFeO_2$-type structure with an *R-3 m* space group symmetry [17–21].

The XRD pattern of the undoped LMNCO cathode exhibits a characteristic peak at 21.0° (2θ), corresponding to the (020) plane of the trigonal crystal system with negligible monoclinic phase contamination as reported in prior studies [17]. The absence of extraneous diffraction peaks confirms the phase purity of the synthesized material. For the In-doped cathode (Fig. 1b), all fundamental reflections of the layered α-$NaFeO_2$ structure remain intact, including the (003), (101), (104), (015), (107), (018), (110), and (113) planes. The preservation of the parent structure's diffraction pattern confirms that In doping occurs *via* isovalent substitution without disrupting the long-range crystalline order. In addition to abovementioned peaks, a new diffraction peak emerges at 31° (marked by asterisk). Based on literature, incorporation of dopant(s) into $Li_{1.2}Mn_{0.54}Ni_{0.13}Co_{0.13}O_2$ cathode is sometimes accompanied with formation of impurity phase(s), which appear(s) as new diffraction peak(s) in XRD patterns. The reason behind formation of impurity phase(s) could be non-homogeneous blending of reaction raw materials [11]. Figure 1c presents the XRD pattern of the Sn-doped LMNCO cathode, showing characteristic reflections of the layered α-$NaFeO_2$ structure between 2θ of 10–75°. A distinct additional peak appears at 27° (marked by asterisk), absent in the undoped material, which is due to formation of impurity phase .

Rietveld refinement analysis was conducted using X'Pert HighScore Plus software to precisely determine the crystallographic parameters of the synthesized cathode materials. Table 1 presents the lattice parameters (*a* and *c*) along with calculated reliability factors for pure LMNCO cathode and its doped analogues incorporating In or Sn cation. The undoped Li-rich NMC cathode material crystallizes in a hexagonal layered structure with lattice parameters of $a = 2.8439$ Å and $c = 14.2128$ Å. Notably, incorporation of either In or Sn dopants induces a systematic expansion of the unit cell, as evidenced by the increased lattice dimensions. This structural modification is particularly significant, as previous studies [22, 23] have demonstrated that such lattice expansion can enhance lithium-ion diffusion kinetics by reducing electrostatic repulsion during Li^+ (de)intercalation

Table 1 The lattice parameters along with reliability factors obtained for the undoped Li-rich cathode and those doped with In or Sn dopant

Sample	Lattice parameters		*c/a* ratio	Reliability factors		
	a (Å)	*c* (Å)		R_{wp} (%)	R_p (%)	χ^2
Pure	2.8439	14.2128	4.9976	8.4	7.1	1.45
Pure + In	2.8460	14.2152	4.9947	8.2	6.8	1.31
Pure + Sn	2.8454	14.2141	4.9954	8.9	7.9	1.57

processes. All investigated compositions maintain a *c/a* ratio exceeding 4.99, confirming the preservation of the characteristic layered structure without significant cation mixing. The observed lattice expansion correlates well with the improved electrochemical performance observed in subsequent cycling tests, suggesting that the dopant-induced structural modifications effectively mitigate the inherent challenges of Li-rich cathodes.

Figure 2 presents the FTIR spectra of the undoped Li-rich cathode material alongside those doped with In or Sn. FTIR spectroscopy was employed to characterize the chemical bonding in the synthesized samples. The FTIR spectrum of the undoped LMNCO cathode, recorded within the wavenumber range of 400–4000 cm^{-1}, exhibits distinct absorption bands between 500 and 750 cm^{-1}. As reported in literature [24, 25], metal–oxygen (M–O) bond stretching vibrations typically appear in the 400–800 cm^{-1} region. Accordingly, the observed vibrational modes within 500–750 cm^{-1} can be attributed to transition metal (TM)–oxygen (O) stretching vibrations. Notably, the FTIR spectrum of the undoped sample reveals no significant peaks beyond those associated with TM–O bonds, indicating minimal additional functional group contributions. In the FTIR spectrum of the In-doped cathode material (Fig. 2), a broad peak is observed near 3500 cm^{-1}, corresponding to the O–H stretching vibration of hydroxyl groups, likely due to adsorbed water molecules [26]. Additionally, the characteristic TM–O bond-related peaks remain evident, though their intensity is reduced compared to the undoped sample. This suggests that In doping influences the vibrational modes of the transition metal-oxygen framework. Similar TM–O bond peaks are also present in the spectrum of the Sn-doped cathode, confirming the retention of the primary metal-oxide structure despite doping.

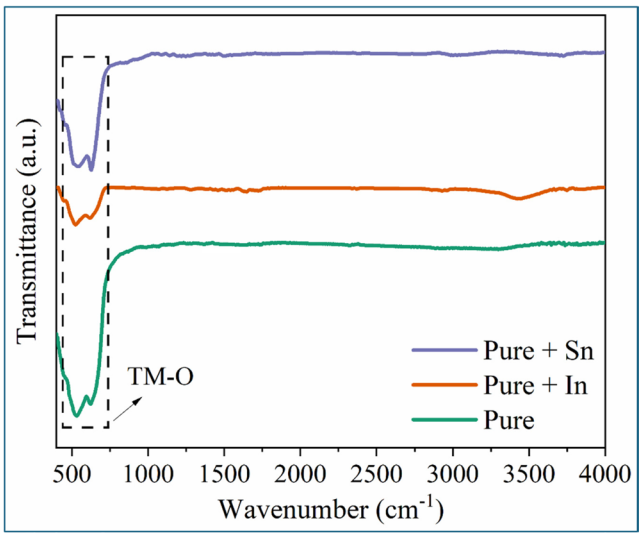

Fig. 2 FTIR spectra of the undoped LMNCO cathode and those doped with In or Sn dopant

Figure 3 presents FESEM images of the pure LMNCO cathode and its In- and Sn-doped counterparts. As shown in Fig. 3a, the undoped Li-rich cathode consists of agglomerated polyhedral nanoparticles with an average particle size of approximately 50 nm. The introduction of In dopant (Fig. 3b) did not induce significant morphological changes, with the polyhedral nanostructure remaining largely unchanged compared to the undoped sample. In contrast, the Sn-doped cathode (Fig. 3c) retained the characteristic polyhedral morphology of the base material, but with the additional presence of nanosized Sn-containing particles dispersed across the surface. These secondary particles, absent in the undoped and In-doped samples, are attributed to Sn incorporation. Notably, FESEM analysis reveals that doping did not substantially alter the overall microstructure of the Li-rich cathode material.

EDXS analysis was employed to analyze the elemental composition of the synthesized cathode materials. As evidenced by the EDXS spectrum of the pure LMNCO cathode material (Fig. 3d), distinct peaks corresponding to the constituent elements - oxygen (O), nickel (Ni), manganese (Mn), and cobalt (Co) - are clearly observed, confirming the expected composition of the undoped Li-rich cathode. Notably, the spectrum shows no detectable signals for In or Sn, indicating the absence of these dopants in the pure cathode material, as anticipated. Figure 3e presents the EDXS spectrum of the In-doped cathode material. In addition to the characteristic peaks of the host material (O, Ni, Mn, and Co) observed in the undoped sample, distinct indium (In) peaks appear in the 3–4 keV range, confirming successful incorporation of the dopant. Similarly, the EDXS spectrum of the Sn-doped LMNCO cathode (Fig. 3f) reveals the expected elemental signatures of the base material along with clear tin (Sn) signals in the 3–4 keV region, providing definitive evidence of Sn doping.

Raman spectroscopy was employed to investigate structural modifications induced by doping cathodic materials with In or Sn. Figure 4a presents the Raman spectrum of the undoped LMNCO cathode material over the wavenumber range of 0–3500 cm^{-1}. A distinct Raman peak is observed at approximately 500 cm^{-1}, corresponding to A_1g mode of *R-3 m* layered structure associated with the symmetric stretching of transition metal-oxygen (TM–O) bonds in the Li-rich cathode structure [25, 27]. The peak relevant to E_g mode at ~470 cm^{-1} appearing commonly in the Raman spectrum of LMNCO is not clearly observed here. Moreover, the broad fluorescence background seen > 1000 cm^{-1} in all cathode materials is ascribed to defect-induced luminescence [27, 28].

Doping with In resulted in peak broadening and a shift toward higher wavenumbers, as evidenced in Fig. 4b. In this regard, the peak of A_1g at ~500 cm^{-1} detected in the Raman

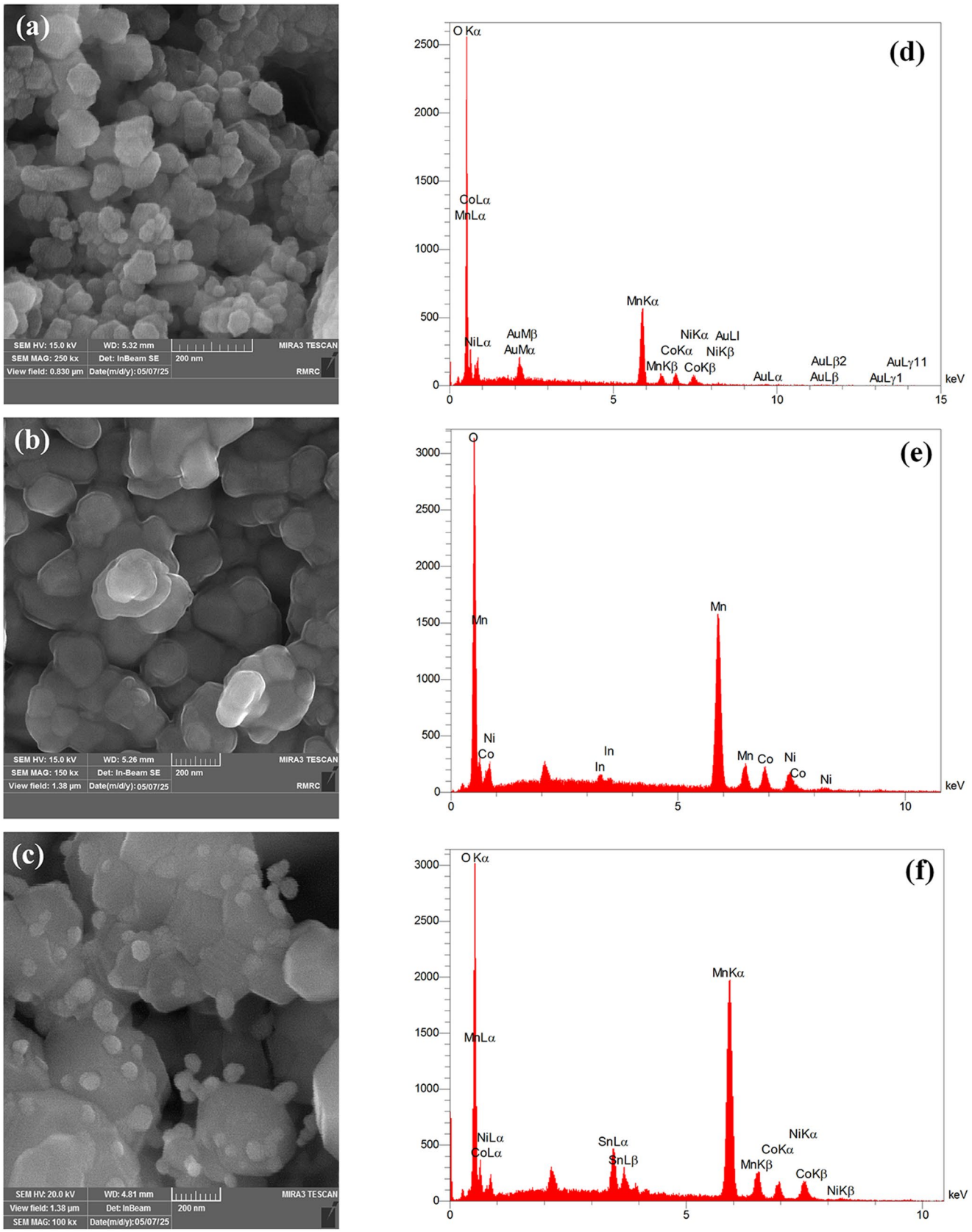

Fig. 3 FESEM images of (**a**) undoped LMNCO cathode and the ones doped with (**b**) In or (**c**) Sn. EDXS patterns of (**d**) undoped LMNCO cathode and the ones doped with (**e**) In or (**f**) Sn

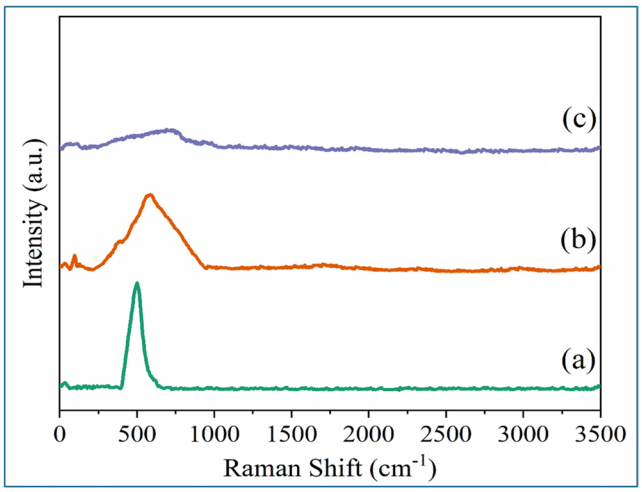

Fig. 4 Raman spectra of (**a**) undoped LMNCO cathode, and the ones doped with (**b**) In, or (**c**) Sn

spectrum of dopant-free cathode shifted to ~600 cm^{-1}. A similar broadening and high-wavenumber shift (from ~500 cm^{-1} to ~750 cm^{-1}) were observed for the Sn-doped cathode (Fig. 4c), suggesting analogous structural perturbations. The characterization results confirm the successful synthesis of the doped cathode materials, with Raman spectroscopy revealing measurable changes in the local bonding environment upon doping.

Electrochemical analyses

CV analysis was employed to evaluate the redox behavior of the synthesized cathode materials. Figure 5 displays the cyclic voltammograms of the undoped LMNCO cathode alongside those doped with In or Sn, recorded within a voltage window of 2.0–5.0 V. In the CV curve of the pure sample, an anodic peak is found at ~4.2 V, which

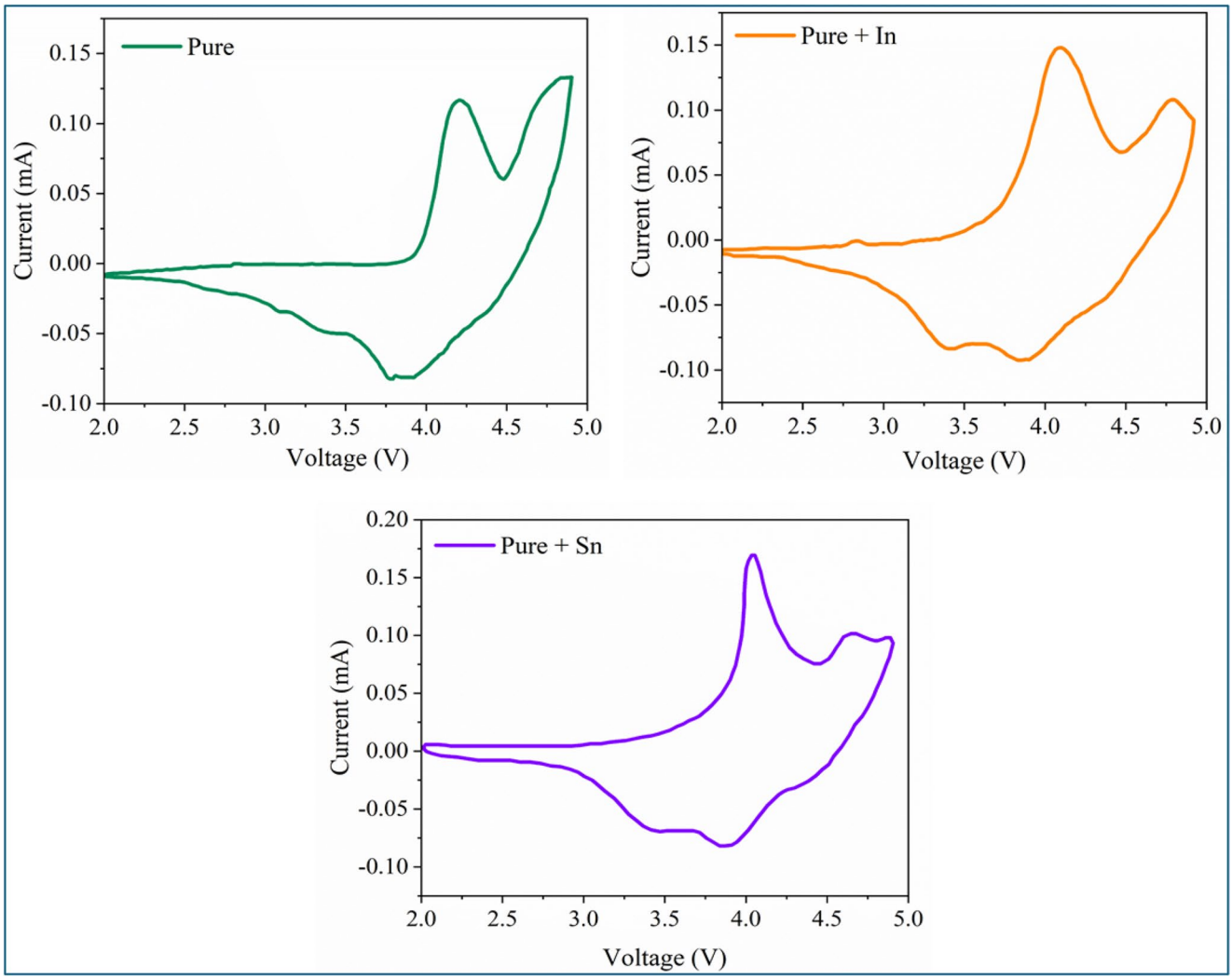

Fig. 5 Cyclic voltammograms of the undoped Li-rich cathode and those doped with In or Sn

originates from the de-insertion of Li^+ ions from the cathode host. In addition to anodic peak, a cathodic peak is observed at ~3.78 V, which arises from the insertion of Li^+ ions. In the cyclic voltammograms of Li-rich cathodes, the anodic and cathodic peaks seen in the voltage varying from 2.5 to 4.5 V are commonly ascribed to the conversion of $Ni^{2+}/Ni^{3+/4+}$ because of two reasons, one of which is that Mn^{4+} ions are not active electrochemically and they do not participate in redox reactions. Additionally, the redox reactions related to $Co^{3+/4+}$ are commonly seen at voltages more than 4.6 V [29].

The reactions pertinent to the conversion of $Ni^{2+}/Ni^{3+/4+}$ are not only the factor taking part in the producing capacity of Li-rich cathodes, but the redox reaction of O^{2-}/O^- oxygen also plays an important role in generating their capacity. The aforementioned reaction typically emerges at voltages more than 4.4 V versus Li/Li^+ and could positively influence the electrochemical performance of the LMNCO cathode [30, 31]. As evidenced by the CV curve of the pure sample, no characteristic peak at >4.4 V showing O^{2-}/O^- redox reactions can be detected. The comparison between CV curves of pure Li rich cathode and the one doped with indium showed that doping affected the intensity of the redox peaks (Fig. 5). Accordingly, the anodic and cathodic peaks arising from $Ni^{2+}/Ni^{3+/4+}$ conversion are detectable. Moreover, the In-doped Li rich cathode shows redox peaks with higher intensity, which pertains to reduction in polarization. Doping pure Li rich cathode with tin also resulted in an increment in its redox peaks. Like other samples, the anodic and cathodic peaks of the $Ni^{2+}/Ni^{3+/4+}$ reaction appeared in the CV curve of the Sn-doped cathode.

As evidenced by the CV analysis, both In- and Sn-doped cathodes exhibit enhanced redox peak intensities compared to the undoped material. This improvement can be attributed to structural modifications induced by doping, as confirmed by Rietveld refinement data. The incorporation of dopant atoms into the Li-rich cathode structure results in lattice expansion, which facilitates Li^+ ion diffusion during insertion/de-insertion processes. This structural effect leads to reduced polarization, as manifested by the sharper redox peaks observed in the doped samples.

The EIS spectra of undoped and doped LMNCO cathodes after the first cycle 0.1 C are presented in Fig. 6a. Nyquist plots for all samples exhibit three distinct regions: (1) a high-frequency intercept representing the electrolyte resistance (R_e), (2) a medium-to-low frequency semicircle corresponding to charge transfer resistance (R_{ct}) at the electrode-electrolyte interface, and (3) a low-frequency Warburg tail (Z_w) indicative of solid-state lithium-ion diffusion. The equivalent circuit model (inset, Fig. 6) incorporates these elements along with a constant phase element (CPE) to account for interfacial inhomogeneity and non-ideal capacitive behavior. Quantitative parameters obtained from the circuit fitting are summarized in Table 2. The R_{ct} values directly reflect the kinetics of the charge transfer process, while the Z_w behavior provides insights into lithium-ion transport within the cathode bulk structure. This comprehensive analysis reveals how In or Sn doping modifies the electrochemical impedance characteristics of the Li-rich cathode materials [32–35].

The fitted impedance parameters (R_e, R_{ct}, and Z_w) are summarized in Table 2. The undoped cathode exhibited a

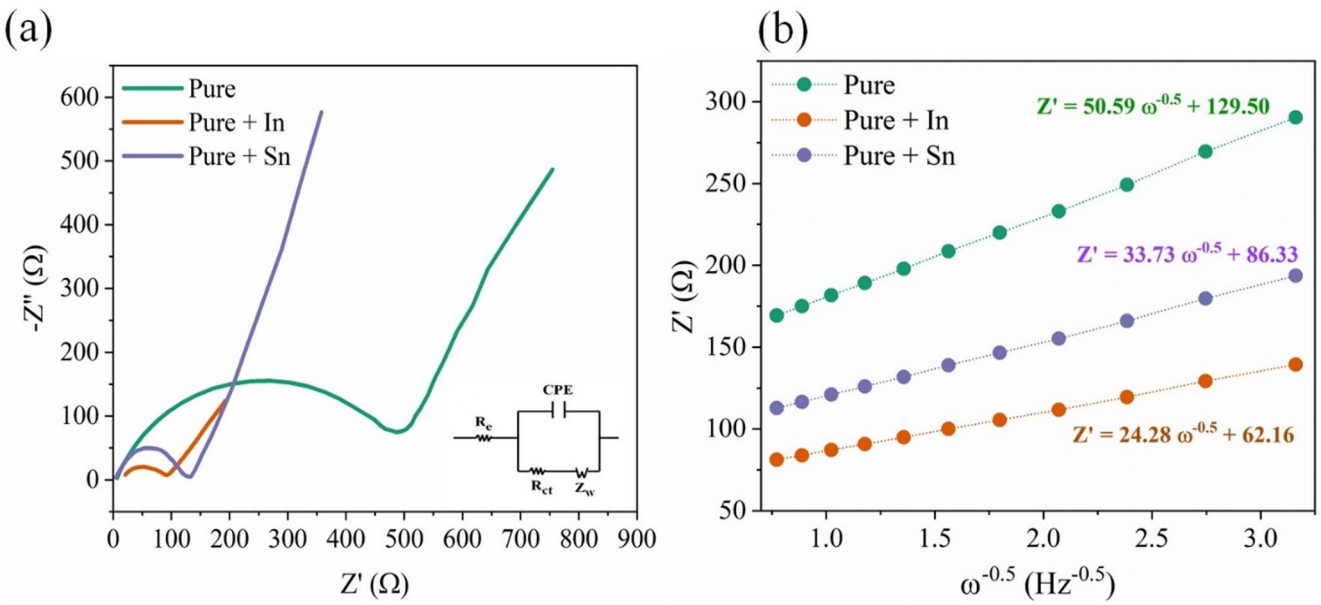

Fig. 6 (**a**) Nyquist plots of undoped LMNCO cathode and the ones doped with indium or tin (inset demonstrates the equivalent circuit). The measurements were carried out after the first cycle 0.1 C. (**b**) the curves of $\omega^{-0.5}$ versus Z' in low-frequency area obtained for prepared electrodes

Table 2 R_e, R_{ct}, and Z_w of pure Li-rich cathode and its counterparts doped with indium or tin

Sample	R_e (Ω)	R_{ct} (Ω)	Z_w (Ω)
Pure	6.6	310.8	0.77
Pure + In	21.2	70.7	0.68
Pure + Sn	4.7	117.4	0.70

substantial charge transfer resistance (R_{ct} = 310.8 Ω), which decreased dramatically to 70.7 Ω upon In doping (77% reduction) and to 117.4 Ω with Sn doping (62% reduction). The Sn-doped cathode demonstrated the lowest electrolyte resistance (R_e = 4.7 Ω), suggesting improved ionic conductivity. Much higher R_e of In-doped compared to undoped and Sn-doped cathodes may be due to fabrication process of electrode. Both dopants significantly reduced the Warburg impedance (Z_w), with the In-doped sample showing the lowest value (0.68 Ω vs. 0.77 Ω for undoped). Eq. 1 was adopted in order to analyze diffusion coefficient (D_{Li+}) of lithium ions [36]:

$$D_{Li^+} = \frac{R^2T^2}{2A^2n^4F^4C^2\sigma^2} \quad (1)$$

Where R indicates gas constant, T signifies absolute temperature, A represents surface area of fabricated electrode, n pertains to the number of electrons by each molecule after intercalation of lithium ion, F is relevant to Faraday constant, C demonstrates the concentration of lithium ions, and σ exhibits Warburg coefficient. Figure 6b renders the linear relationship between Z' in the low-frequency region and $\omega^{-0.5}$. The σ in Eq. 1 equals to the slope of the curve of Z' versus $\omega^{-0.5}$, which has indirect relationship with D_{Li+} ($D_{Li+} = 1/\sigma^2$) [36]. By considering all parameters of R, T, A, n, F, and C constant, D_{Li+} of In-doped and Sn-doped cathodes are approximately 4.34 and 2.25 times of D_{Li+} of pure cathode, respectively.

This systematic decrease in both R_{ct} and Z_w and also increase in diffusion coefficient of lithium ions indicate enhanced charge transfer kinetics and improved Li^+ solid-state diffusion. The improved electrochemical performance can be attributed to the lattice expansion induced by dopant incorporation, which facilitates Li^+ insertion/de-insertion processes. The expanded crystal structure reduces steric hindrance for ionic movement while maintaining structural stability during cycling.

Figure 7 demonstrates the initial charge and discharge diagrams of the undoped LMNCO cathode and its counterparts doped with indium or tin. Half-cells made up of synthesized cathodes as the working electrode and Li metal as the counter electrode were utilized in order to record the initial charge and discharge curves. Table 3 tabulates charge capacity, discharge capacity, and Coulombic efficiency (CE) of the case study samples.

Table 3 demonstrates that the undoped LMNCO cathode exhibited initial electrochemical characteristics with

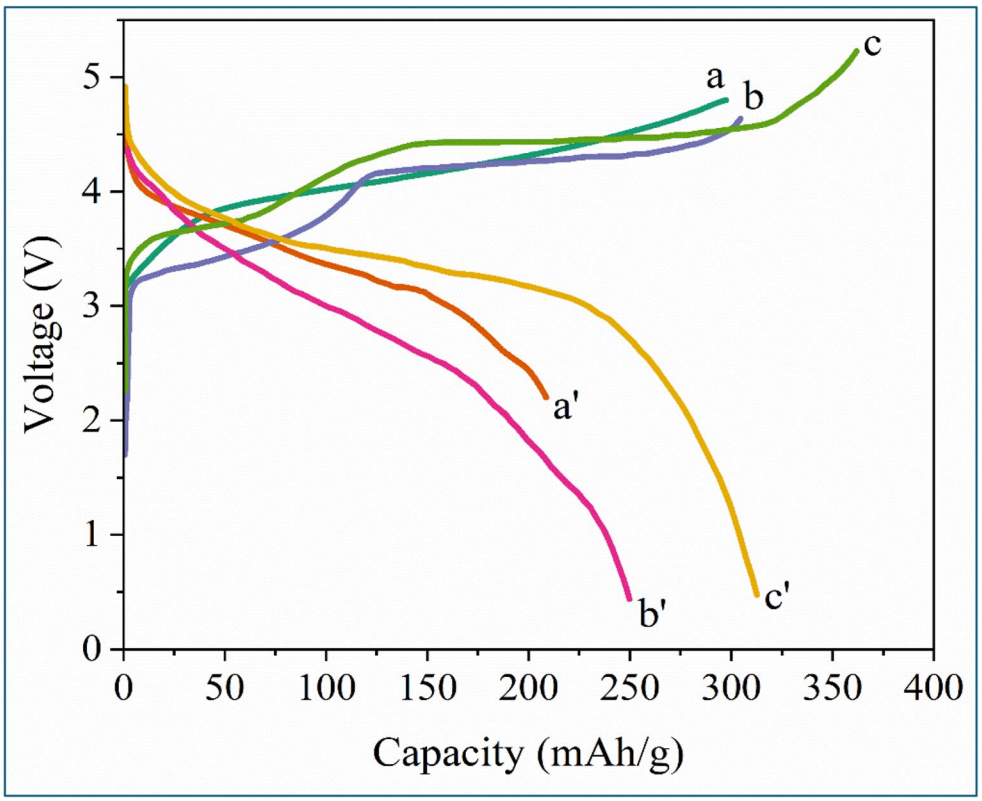

Fig. 7 The initial charge/discharge diagrams of (a, a') pure LMNCO cathode and the ones doped with (b, b') In or (c, c') Sn

Table 3 Electrochemical performance of pure and doped LMNCO cathodes during the first cycle at 0.1 C rate

Sample	Charge capacity (mAh/g)	Discharge capacity (mAh/g)	Coulombic efficiency (%)
Pure	297.5	208.7	70.1
Pure + In	304.7	249.8	81.9
Pure + Sn	362	312.6	86.3

a charge capacity of 297.5 mAh/g and discharge capacity of 208.7 mAh/g, yielding a Coulombic efficiency of 70.1%. The plateau appearing between 4 and 4.5 V in the charge curve of undoped cathode is imputed to activation of Li_2MnO_3 and structural rearrangement [11]. Following indium doping, the modified cathode showed enhanced performance metrics, achieving a charge capacity of 304.7 mAh/g and discharge capacity of 249.8 mAh/g, corresponding to an improved Coulombic efficiency of 81.9%. The characteristic plateau demonstrating activation of Li_2MnO_3 at 4.5 V is also seen in charge curves of In- and Sn-doped cathodes. The Sn-doped cathode demonstrated better electrochemical performance compared to other prepared samples, exhibiting the highest charge capacity (362 mAh/g) and discharge capacity (312.6 mAh/g), corresponding to a Coulombic efficiency of 86.3%.

The cycling performance of undoped and doped electrodes are depicted in Fig. 8a. Accordingly, the discharge capacities delivered by dopant-free, In-doped, and Sn-doped electrodes respectively were 195.2, 244, and 308.9 mAh/g after 10 cycles 0.1 C. In addition to cycling performance, the rate capability of electrodes was examined at different C-rates (see Fig. 8b). In this regard, the Sn-doped electrode delivered approximately discharge capacities of 313, 305, 295, 285, and 275 mAh/g respectively at C-rates of 0.1 C, 0.2 C, 0.5 C, 1 C, and 2 C.

The enhanced performance of Sn- and In-doped LMNCO materials is attributed to the effective role of Sn or In doping in facilitating lithium ion insertion/extraction through enlarging crystal lattices, which reduces electrode resistance and consequently improves charge/discharge capacities.

As shown in Table 4, the electrochemical performance of our Sn-doped LMNCO cathode demonstrates significant improvements when compared to previously reported modified systems.

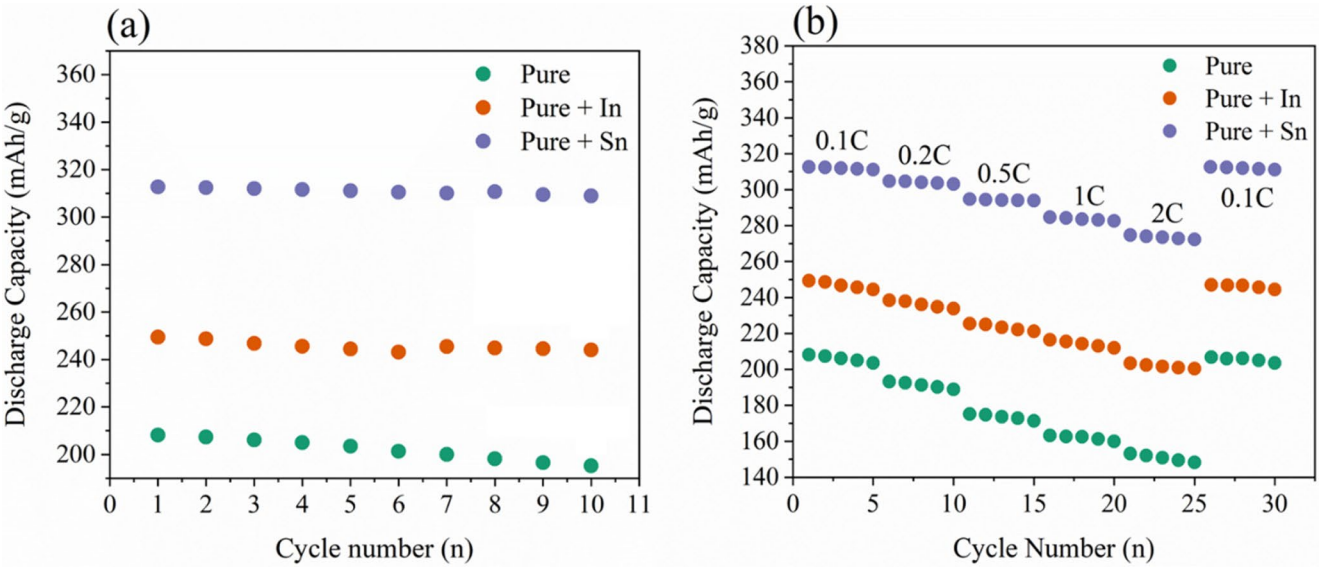

Fig. 8 (**a**) cycling performance, and (**b**) rate capability of the synthesized electrodes

Table 4 Comparative electrochemical performance of Sn-doped LMNCO cathodes at 0.1 C rate (1st cycle). All reported studies used the same base composition for comparison

Dopant	Coating agent	Compositing agent	Voltage (V)	Charge capacity (mAh/g)	Discharge capacity (mAh/g)	CE (%)	Ref.
Nb	-	-	2.0–4.8	343.2	267.7	78	[37]
Er	-	-	2.0–4.8	344.1	271.5	78.9	[38]
Al	-	-	2.0–4.8	321.5	253.7	78.9	[39]
Sn	-	-	1.8–4.8	362	312.6	86.3	This work

Conclusions

In this study, we successfully synthesized Li-rich LMNCO cathode material and systematically investigated the effects of In or Sn doping through comprehensive structural and electrochemical characterization. XRD analysis confirmed the preservation of the layered α-$NaFeO_2$ structure in all samples while revealing distinct dopant-related peaks at 31° (In-doped) and 27° (Sn-doped), verifying successful incorporation of dopant ions. FTIR spectroscopy detected characteristic TM-O bond vibrations, and Raman spectra showed the A_1g symmetric stretching mode of TM-O bonds, both confirming successful material synthesis. FESEM imaging demonstrated that doping had negligible effects on nanoparticle morphology. Electrochemical characterization revealed significant performance enhancement in doped samples. Both CV and EIS analyses showed reduced charge transfer polarization, attributed to improved Li^+ ion mobility through dopant-induced lattice expansion.

Among all fabricated electrodes, the one doped with Sn exhibited the best electrochemical performance. In this regard, it reached discharge capacity of 308.9 mAh/g after 10 cycles. Moreover, Sn-induced electrode delivered discharge capacity of 313, 305, 295, 285, and 275 mAh/g respectively at C-rates of 0.1 C, 0.2 C, 0.5 C, 1 C, and 2 C. These electrochemical propertiescould position the Sn-doped Li-rich cathode as a highly promising candidate for advanced energy storage applications. The demonstrated effectiveness of Sn doping in facilitating charge transfer processes suggests this approach could be valuable for developing next-generation high-performance cathode materials.

Acknowledgements The authors appreciate the support of the Ferdowsi University of Mashhad.

Author contributions Reihane Etefagh: Formal analysis, Data curation, Validation, Writing – original draft. Amirhassan Amiri: Supervision, Funding acquisition, Writing – review & editing. Boshra Ghanbari Shohany: Investigation, Data curation, Writing – original draft. Nima Rasekh Saleh: Supervision, Writing – review & editing.

Data availability No datasets were generated or analysed during the current study.

Declarations

Competing interests The authors declare no competing interests.

References

1. Silvestri L et al (2023) Li-rich layered oxides: structure and doping strategies to enable Co-poor/Co-free cathodes for Li-ion batteries. Crystals 13(2):204
2. Yang R et al (2021) A first-principles study on the properties of Sn-doped LiCoO 2 for Li-ion batteries. Dalton Trans 50(13):4680–4685
3. Leifer N et al (2020) Linking structure to performance of Li 1.2 Mn 0.54 Ni 0.13 Co 0.13 O 2 (Li and Mn rich NMC) cathode materials synthesized by different methods. Phys Chem Chem Phys 22(16):9098–9109
4. Chen C et al (2016) Oxygen vacancies in SnO2 surface coating to enhance the activation of layered Li-Rich Li1. 2Mn0. 54Ni0. 13Co0. 13O2 cathode material for Li-ion batteries. J Power Sources 331:91–99
5. Zubair M et al (2018) Electrochemical kinetics and cycle stability improvement with Nb doping for lithium-rich layered oxides. ACS Appl Energy Mater 2(1):503–512
6. Zhang W et al (2019) Surface modification of Li1. 2Mn0. 54Ni0. 13Co0. 13O2 cathode material with Al2O3/SiO2 composite for lithium-ion batteries. J Electrochem Soc 166(6):A863
7. Liu W et al (2015) Nickel-rich layered lithium transition-metal oxide for high-energy lithium-ion batteries. Angew Chem Int Ed 54(15):4440–4457
8. Zhu H et al (2020) Sn-doping and Li2SnO3 nano-coating layer co-modified LiNi0. 5Co0. 2Mn0. 3O2 with improved cycle stability at 4.6 V cut-off voltage. Nanomaterials 10(5):868
9. Kantichaimongkol P, Wanotayan T (2025) Review on surface engineering of NMC for high performance of lithium-ion batteries. J Met Mater Minerals 35(2):e2338–e2338
10. Zhou L et al (2017) Sn-doped Li1. 2Mn0. 54Ni0. 13Co0. 13O2 cathode materials for lithium-ion batteries with enhanced electrochemical performance. J Solid State Electrochem 21(12):3467–3477
11. Li B et al (2019) Improving rate performances of Li-rich layered oxide by the co-doping of Sn and K ions. J Materiomics 5(2):149–155
12. Wang D et al (2018) Integrated surface functionalization of Li-rich cathode materials for Li-ion batteries. ACS Appl Mater Interfaces 10(48):41802–41813
13. Dalapati GK et al (2021) Tin oxide for optoelectronic, photovoltaic and energy storage devices: a review. J Mater Chem A 9(31):16621–16684
14. Lin W et al (2023) Indium doping: an effective route to optimize the electrochemical performance of lifepo4 cathode material. Solid State Ionics 403:116322
15. Luo Z (2025) A Review on element doping in Li-rich cathode materials for lithium-ion batteries. in E3S Web of Conferences. EDP Sciences
16. Bai G et al (2022) Electrochemical behavior of Sn-doped Li1. 2V3O8 cathode materials for Lithium-ion batteries. Mater Sci Engineering: B 286:115988
17. Çetin B, Camtakan Z, Yuca N (2020) Synthesis and characterization of li-rich cathode material for lithium ion batteries. Mater Lett 273:127927
18. Zhang K et al (2020) Improving electrochemical properties by sodium doping for lithium-rich layered oxides. ACS Appl Energy Mater 3(9):8953–8959
19. Vanaphuti P et al (2019) Enhanced electrochemical performance of the lithium-manganese-rich cathode for Li-ion batteries with Na and F codoping. ACS Appl Mater Interfaces 11(41):37842–37849
20. Shi Y et al (2020) Facile and scalable dry surface doping technique to enhance the electrochemical performance of $LiNi_{0.64}Mn_{0.2}Co_{0.16}O_2$ cathode materials. J Mater Chem A 8(38):19866–19872
21. Liu S et al (2018) Comparative studies of zirconium doping and coating on $LiNi_{0.6}Co_{0.2}Mn_{0.2}O_2$ cathode material at elevated temperatures. J Power Sources 396:288–296
22. Darjazi H et al (2022) Improving high-voltage cycling performance of nickel-rich NMC layered oxide cathodes for

rechargeable lithium–ion batteries by Mg and Zr co-doping. Mater Today Sustain 20:100236
23. Darjazi H et al (2022) Improvement of structural and electrochemical properties of NMC layered cathode material by combined doping and coating. Electrochim Acta 404:139577
24. Pasieczna-Patkowska S, Cichy M, Flieger J (2025) Application of Fourier transform infrared (FTIR) spectroscopy in characterization of green synthesized nanoparticles. Molecules 30(3):684
25. Jeevanantham B et al (2022) Magnesium doped $LiNi_xMn_yCo_zO_2$ cathode-structural properties. Appl Surf Sci Adv 12:100350
26. Tkachenko Y, Niedzielski P (2022) FTIR as a method for qualitative assessment of solid samples in geochemical research: a review. Molecules 27(24):8846
27. He D et al (2023) Structural insights into lithium-deficient type Li-rich layered oxide for high-performance cathode. Chin J Struct Chem 42:100060
28. Li LT et al (2023) Synthesis of high-performance single-crystal Li-rich cathode by self-combustion method. Rare Met 42(3):830–837
29. Hashem AM et al (2019) Doped nanoscale NMC333 as cathode materials for Li-ion batteries. Materials 12(18):2899
30. Celeste A et al (2023) Unravelling structural changes of the Li1.2Mn0. 54Ni0. 13Co0. 13O2 lattice upon cycling in lithium cell. Mater Today Sustain 21:100277
31. Zhao S et al (2021) Reaction mechanisms of layered lithium-rich cathode materials for high-energy lithium-ion batteries. Angew Chem Int Ed 60(5):2208–2220
32. Yavarinasab A et al (2021) Potentiodynamic electrochemical impedance spectroscopy of polyaniline-modified pencil graphite electrodes for selective detection of biochemical trace elements. Polymers 14(1):31
33. Kim C, Jang I (2025) Application of Electrochemical Impedance Spectroscopy for Diagnostics in Fuel Cells, Electrolyzers, and Batteries. ChemElectroChem 12(11):e202500005
34. Kasper M et al (2023) Calibrated electrochemical impedance spectroscopy and time-domain measurements of a 7 kWh automotive lithium-ion battery module with 396 cylindrical cells. Batteries Supercaps 6(2):e202200415
35. Kannan DR, Weatherspoon M (2021) The effect of pulse charging on commercial lithium cobalt oxide (LCO) battery characteristics. Int J Electrochem Sci 16(4):210453
36. Keshmarzi MK, Fathollahi Zonouz A, Poursalehi F, Mosallanejad B, Daryakenari AA (2020) Electrophoretic deposition of nanographitic flakes/Co_3O_4 nanocomposite layers synthesized by solvothermal process for improved lithium-ion-battery anode. J Solid State Chem 288:121471
37. Xu Y, Cui Q (2020) Nb-doped Li1. 20 [Mn0. 54Ni0. 13Co0. 13] O2 cathode material with enhanced electrochemical properties for lithium-ion battery. Int J Electrochem Sci 15(1):803–815
38. Shicheng W, Ling J, Xiaowen T (2017) Synthesis and electrochemical properties of Er^{3+} Doped $Li[Li_{0.2}Mn_{0.54}Ni_{0.13}Co_{0.13}]O_2$ as Cathode Materials for Lithium Ion Bateries. Int J Electrochem Sci 12:10783–10790
39. Luo M et al (2018) Effects of doping Al on the structure and electrochemical performances of $Li[Li_{0.2}Mn_{0.54}Ni_{0.13}Co_{0.13}]O_2$ cathode materials. Ionics 24:967–976